Research article

Brian S. Lee, Bumho Kim, Alexandre P. Freitas, Aseema Mohanty, Yibo Zhu, Gaurang R. Bhatt, James Hone and Michal Lipson*

High-performance integrated graphene electro-optic modulator at cryogenic temperature

https://doi.org/10.1515/nanoph-2020-0363
Received July 2, 2020; accepted September 8, 2020; published online September 25, 2020

Abstract: High-performance integrated electro-optic modulators operating at low temperature are critical for optical interconnects in cryogenic applications. Existing integrated modulators, however, suffer from reduced modulation efficiency or bandwidth at low temperatures because they rely on tuning mechanisms that degrade with decreasing temperature. Graphene modulators are a promising alternative because graphene's intrinsic carrier mobility increases at low temperature. Here, we demonstrate an integrated graphene-based electro-optic modulator whose 14.7 GHz bandwidth at 4.9 K exceeds the room temperature bandwidth of 12.6 GHz. The bandwidth of the modulator is limited only by high contact resistance, and its intrinsic RC-limited bandwidth is 200 GHz at 4.9 K.

Keywords: 2D materials; cryogenic; graphene; modulator; ring resonator; silicon photonics.

1 Introduction

Integrated electro-optic modulators are essential for high-bandwidth optical links in cryogenic environments, in applications such as delivering control signals and reading out data in solid-state quantum computing [1–6] or inter-satellite optical communications [7, 8]. For example, superconducting nanowire single-photon detectors offer exceptional performance but require optical modulators operating at cryogenic environment to readout signals to room temperature [1, 4]. Superconducting single-flux quantum circuits provide operating frequencies approaching 770 GHz and are expected to provide superior computing performance to conventional electronics at room temperature [6]. Yet, interfacing cryogenic systems to room temperature controllers and processors with electrical connections pose several issues, such as increased thermal load to the cryogenic environment, which potentially degrades cryogenic circuit performance because of increased thermal noise and limited bandwidth due to high frequency losses. Therefore, there is an increasing demand for optical interconnects to interface cryogenic and room temperature systems, and modulators operating at cryogenic temperature are an essential component for establishing such an optical link.

Existing electro-optic modulators, however, suffer from low bandwidth or reduced modulation efficiency at cryogenic temperatures because they rely on tuning mechanisms that degrade with decreasing temperature. Devices based on free carriers such as silicon modulators [9], for example, suffer from carrier freeze-out at low temperature [10]. This may be mitigated with degenerate doping but at the cost of increased insertion loss. Non–carrier-based modulators using Franz–Keldysh or quantum-confined Stark effect [11] or Pockels effect [12] suffer from weak electro-optic strength at low temperature, thus requiring higher drive voltage and increased footprint, which limits the integration density of photonic integrated circuits for cryogenic applications.

Graphene modulators are a promising alternative for low-temperature applications. They rely on tuning graphene's absorption through electrostatic gating [13], a mechanism which does not suffer from degradation at low temperatures [14, 15]. The intrinsic electronic mobility of graphene increases on cooling [16–18], such that the speed, determined by the RC charging time, should not intrinsically degrade at low temperature. However, no work has demonstrated low-temperature operation of

*Corresponding author: Michal Lipson, Department of Electrical Engineering, Columbia University, New York, NY 10027, USA, E-mail: ml3745@columbia.edu
Brian S. Lee, Aseema Mohanty and Gaurang R. Bhatt, Department of Electrical Engineering, Columbia University, New York, NY 10027, USA. https://orcid.org/0000-0002-8040-3576 (B.S. Lee)
Bumho Kim, Yibo Zhu and James Hone, Department of Mechanical Engineering, Columbia University, New York, NY 10027, USA
Alexandre P. Freitas, School of Electrical and Computer Engineering, University of Campinas, Campinas-SP, 13083-970, Brazil. https://orcid.org/0000-0003-1474-5938

graphene modulators to date. Here, we demonstrate a high-bandwidth graphene electro-optic modulator at 4.9 K. The mobility of the graphene in these devices increases with decreasing temperature, leading to reduced device resistance and better RC-limited bandwidth of graphene modulators. Therefore, graphene enables high-speed integrated electro-absorption modulator that naturally exhibits a high bandwidth at cryogenic temperature.

2 Graphene-silicon nitride electro-absorption ring modulator

The graphene electro-absorption modulator consists of a dual-layer graphene capacitor integrated with a silicon nitride (Si_3N_4) waveguide. The capacitor consists of two graphene sheets (cyan solid lines in Figure 1A) separated by 30 nm alumina (Al_2O_3) gate dielectric (white solid lines in Figure 1A are boundaries of Al_2O_3 gate dielectric, Si_3N_4 waveguide, and metals). The Si_3N_4 waveguide (1300 nm by 330 nm) is designed to ensure significant overlap between the fundamental quasi-transverse electric (quasi-TE) mode and graphene capacitor via evanescent wave as shown in Figure 1A. By applying voltage to the graphene capacitor, we electrostatically gate the graphene sheets and induce Pauli-blocking, that is, reduce optical absorption and mode propagation loss by suppressing interband transitions of carriers in graphene [19]. We describe the fabrication steps of the Si_3N_4 waveguide and dual-layer graphene capacitor in Figure S1 in the *Supplementary material*.

We embed the graphene capacitor/Si_3N_4 waveguide in a ring resonator as shown in Figure 1B to enhance graphene–light interaction while reducing footprint and capacitance for maximum bandwidth. In addition, we use resonator loss modulation at critical coupling [20, 21] to achieve strong modulation even with small voltage swing and small capacitance (about 9 fF, see the optical micrograph inset of Figure 1C for device scale). Figure 1C shows the simulated transmission through the waveguide (blue curve, left axis) and slope of transmission (orange curve, right axis) with respect to resonator round trip loss. The transmission is most sensitive (i.e., largest slope) when the resonator is near critical coupling (i.e., near the dashed vertical line in Figure 1C). We therefore design the resonator–bus coupling gap (around 180 nm) to be near critical coupling to achieve highest sensitivity to changes in graphene absorption and to transition from being critically coupled to overcoupled as graphene absorption is modulated from high to low, respectively.

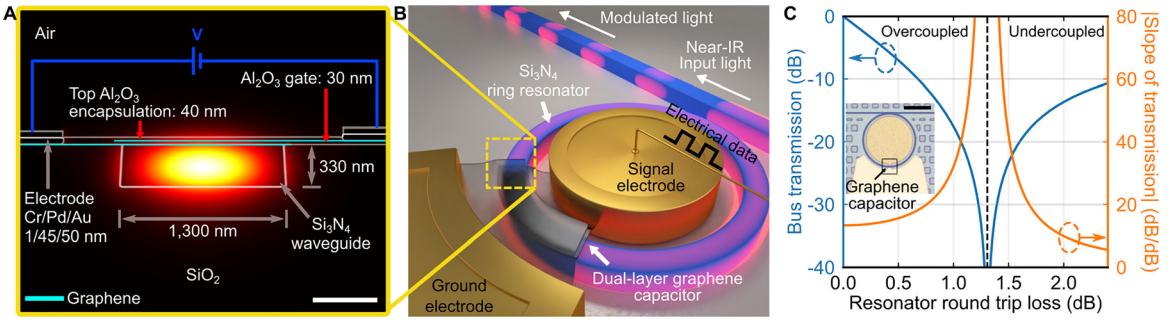

Figure 1: Graphene electro-absorption modulator design and resonator loss modulation at critical coupling.
(A) The graphene modulator consists of a dual-layer graphene capacitor on top of a Si_3N_4 waveguide. The capacitor consists of two graphene sheets (cyan solid lines) separated by a 30 nm Al_2O_3 gate dielectric (white solid lines are boundaries for Al_2O_3 gate dielectric, Si_3N_4 waveguide, and metals). The top graphene sheet is cladded with 40 nm Al_2O_3. The Si_3N_4 waveguide (1300 nm by 330 nm) is designed to ensure significant overlap between the fundamental quasi-TE mode and graphene capacitor via evanescent wave. By applying voltage between the graphene sheets, we electrostatically gate them and induce Pauli-blocking, suppressing interband transitions of carriers in graphene sheets and reducing optical absorption and mode propagation loss. White scale bar, 200 nm. (B) The graphene capacitor is embedded in a ring resonator to enhance graphene–light interaction while reducing footprint and capacitance for maximum bandwidth. (C) Simulated transmission (blue curve, left axis) and slope of transmission (orange curve, right axis) with respect to resonator round trip loss. To achieve strong modulation even with small voltage swing and small capacitance, we modulate resonator loss near critical coupling shown as dashed vertical line. The transmission is most sensitive (i.e., largest slope) when the resonator is near critical coupling. We, therefore, design the resonator–bus coupling gap (around 180 nm) to be near critical coupling. The modulator transitions from being critically coupled to overcoupled as graphene absorption is modulated from high to low, respectively. Inset: An optical micrograph of the fabricated device showing the waveguide and ring resonator, false-colored in blue. The two electrodes for the graphene capacitor are shown in yellow. Boxed region indicates where the graphene capacitor is placed with 5-μm device length around the ring with 40 μm radius. Squares around the device are fill patterns for chemical mechanical planarization. Black scale bar, 40 μm.

3 Results

We show modulation of transmission by more than 7 dB at room temperature by electrostatically gating the graphene and, thus, modulating the resonator round trip loss near critical coupling. In Figure 2A, we show the transmission spectra of the graphene ring modulator at different applied voltages. The transmission is about −25 dB at resonance (around 1586.2 nm) when applied voltage is 0 V, indicating near critical coupling of the ring with high graphene absorption. With applied voltage to the graphene modulator, the resonator–bus coupling condition becomes more overcoupled and the transmission at resonance increases. To measure the change in resonator round trip loss as a function of voltage, we measure the loaded quality factor Q_L from each of the spectra shown in Figure 2A and plot it in Figure 2B. The Q_L increases from about 3500 to 3700 over 9 V, corresponding to resonator round trip loss decreasing from 1.10 to 0.96 dB [22] due to decreasing graphene absorption. We measure Q_L of the ring resonator without graphene sheets to be around 4700 for strongly overcoupled resonator (see Figure S2 in the *Supplementary material*). Therefore, we do not completely achieve Pauli-blocking in our graphene sheets. We attribute this to the lower-than-designed dielectric constant of our atomic layer deposition Al_2O_3 gate, $\varepsilon_{Al_2O_3} = 4.2$ (Figure S3D in the *Supplementary material*). With optimized gate quality, we expect to reach further into the Pauli-blocking regime and achieve higher extinction ratio (see Figure S4 in the *Supplementary material*).

We characterize the frequency response of the graphene modulator at 293 and 4.9 K and measure a 3-dB bandwidth of 12.6 and 14.7 GHz, respectively (Figure 3). We place the graphene modulator in a cryogenic probe station to precisely control the temperature of the chip and perform high-speed electro-optic measurements (see Figure S5 for experimental setup at cryogenic temperature). The bandwidth increases approximately 16% when the device is cooled from room to cryogenic temperature despite being driven with the same d.c. bias (−9 V) and RF power (13.5 dBm, $V_{pp} = 3$ V, see Figure S6 for eye diagrams measured at 293 K in the *Supplementary material*). We normalize the amplitude of each curve to the response at 1 MHz and fit it to a single-pole transfer function $1/(1 + j2\pi f\tau)$, where f is the frequency and τ is the modulator time constant. The 3-dB bandwidth at each temperature is measured from the fitted curve (shown as dashed lines in Figure 3) as $f_{3dB} = 1/(2\pi\tau)$. We do not observe significant change in modulation efficiency at low temperature in agreement with Li et al. who have measured at $T = 45$ K [14]. We suspect that the Pauli-blocking transition becomes negligibly steeper even at cryogenic temperatures due to short lifetimes of excited carriers in graphene on time scales of 100 fs [23, 24].

We show that the increase of graphene modulator's bandwidth at low temperature follows the trend of graphene carrier mobility. We pattern graphene test devices into Hall bar configuration, allowing extraction of the carrier mobility by simultaneous measurement of the four-terminal conductance and carrier density through the Hall effect (see Figure S3 in the *Supplementary material*). As shown in Figure 4A, the mobility increases from approximately 1420 cm^2/V s at 293 K to 1650 cm^2/V s at 4.9 K. This increase reflects the weakening of scattering from phonons

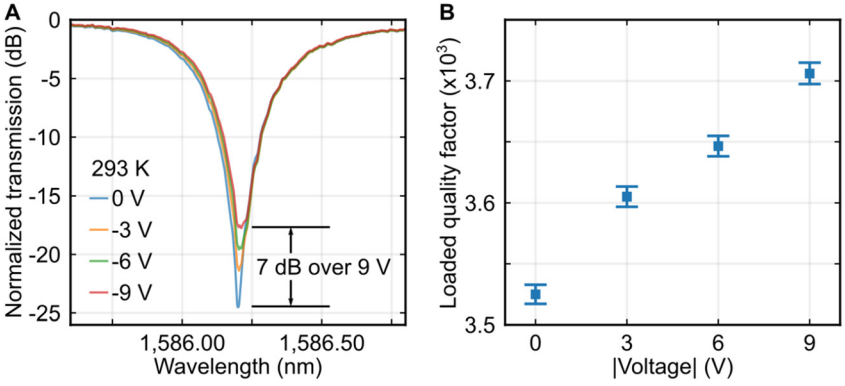

Figure 2: Modulating resonator–bus coupling condition by electrostatically gating the graphene capacitor.
(A) Transmission spectra of the modulator at various d.c. voltages at room temperature. With applied voltage to the graphene modulator, we change the transmission at resonance by more than 7 dB by decreasing graphene absorption and changing the resonator–bus coupling condition. By reducing graphene absorption and resonator round trip loss, we make the resonator more overcoupled as indicated by the increasing transmission at resonance. (B) We measure the loaded quality factor Q_L of the resonator spectra in Figure 2A. The Q_L increases from about 3500 to 3700 over 9 V, corresponding to resonator round trip loss decreasing from 1.10 to 0.96 dB due to decreasing graphene absorption.

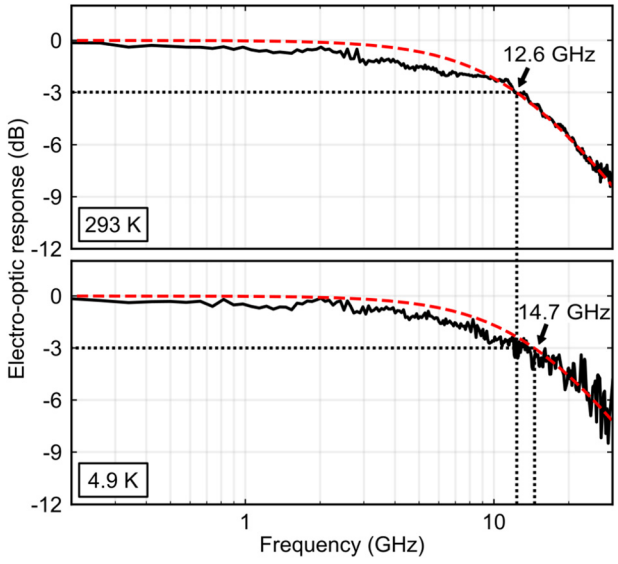

Figure 3: Enhancement of electro-optic bandwidth of graphene modulator at cryogenic temperature.
The measured electro-optic bandwidth at 293 and 4.9 K are 12.6 and 14.7 GHz, respectively. The red dashed lines are single pole fitting to the data. The electro-optic response increases by about 16% when the device is cooled from room to cryogenic temperature. The modulator is driven with a vector network analyzer (see Figure S5 in the *Supplementary material*) with RF power 13.5 dBm (V_{pp} = 3 V) at d.c. bias of –9 V at both temperatures.

in the graphene and the surrounding Al_2O_3 dielectric. The solid line in Figure 4A shows a fit to the data which combines temperature-independent scattering from disorder (such as trapped charge in the Al_2O_3) and temperature-dependent scattering from graphene longitudinal acoustic phonons and Al_2O_3-graphene surface polar phonons [16–18, 25] (see Figure S7 in the *Supplementary material*). To confirm that the device's resistance governs the bandwidth change with temperature, we verify that the capacitance remains constant with temperature. The capacitance changes by less than 5% from 293 to 1.5 K by measuring the change in carrier concentration of the graphene Hall bar at various temperatures (see Figure S8 in the *Supplementary material*).

4 Discussion

Using the measured mobility and two-terminal device resistance, we determine that the graphene modulator bandwidth is currently limited by its high contact resistance of around 2.3 ± 1.2 Ω μm (see Figure S9 in the *Supplementary material*), whereas its high mobility (and resulting low sheet resistance) at cryogenic temperature supports a fundamental bandwidth of 200 GHz. From the RC circuit in Figure 4B, the modulator's total RC-limited bandwidth is,

$$f_{3\mathrm{dB}} = \frac{1}{2\pi(2R_c + 2R_{\mathrm{sh}}g)C}, \tag{1}$$

where R_c is the contact resistance, R_{sh} is the sheet resistance, g is the gap between the electrodes and capacitor,

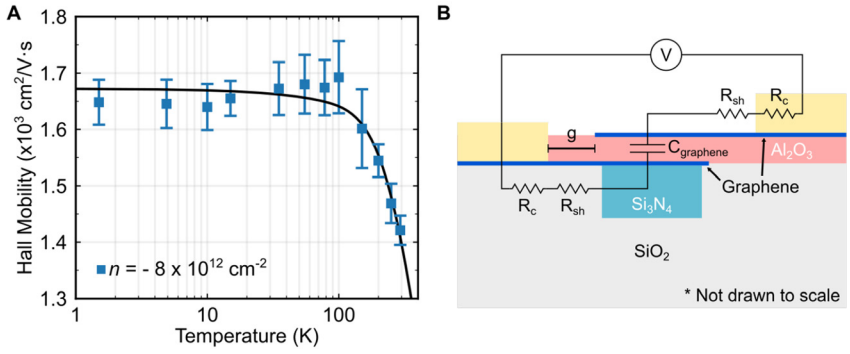

Figure 4: Mobility enhancement of graphene at cryogenic temperature and its correspondence to graphene modulator.
(A) We extract graphene mobility using a Hall bar (see Figure S3 in the *Supplementary material*) with respect to temperature. We measure an increase of mobility from approximately 1420 $cm^2/V\,s$ at 293 K to 1650 $cm^2/V\,s$ at 4.9 K. This increase reflects the weakening of scattering from phonons in the graphene and the surrounding Al_2O_3 dielectric. The black solid line shows a fit to the data which combines temperature-independent scattering from disorder (such as trapped charge in the Al_2O_3) and temperature-dependent scattering from graphene longitudinal acoustic phonons and Al_2O_3-graphene surface polar phonons (see Figure S7 in the *Supplementary material*). The measured mobility follows the temperature dependence of the fitted curve well within the measurement error. (B) The equivalent RC circuit of the graphene modulator is overlaid with the device cross section. R_c is the graphene contact resistance, R_{sh} is the graphene sheet resistance, C is the dual-layer graphene capacitor, and g is the gap between the electrode and the capacitor. The enhancement of graphene carrier mobility at cryogenic temperature reduces the sheet resistance of the device, increasing the RC-limited bandwidth.

and C is the capacitance per length. The total bandwidth is governed by contributions from extrinsic (i.e., due to parasitic components) and intrinsic bandwidth:

$$1/f_{3\mathrm{dB}} = 1/\mathrm{BW}_{\mathrm{ext}} + 1/\mathrm{BW}_{\mathrm{int}} = 2\pi(2R_cC) + 2\pi(2R_{\mathrm{sh}}gC), \quad (2)$$

where $\mathrm{BW}_{\mathrm{ext}} = 1/(2\pi[2R_cC])$ is the extrinsic bandwidth governed by parasitic contact resistance and $\mathrm{BW}_{\mathrm{int}} = 1/(2\pi[2R_{\mathrm{sh}}gC])$ is the intrinsic device bandwidth governed by the capacitance and sheet resistance. From Hall bar measurements (see Figure S3 in the *Supplementary material*) and using Equation (1), we extract C and R_{sh} at 4.9 K as 1.85 fF/μm and 470 Ω/sq, respectively, which translates to $\mathrm{BW}_{\mathrm{int}}$ = 200 GHz. The high contact resistance can be attributed to the ungated contact regions. Unlike electronics, it is challenging to gate graphene contact regions in photonic devices as metal gates could induce unwanted optical absorption, or extending the graphene capacitor sheets to the contacts will parasitically increase the capacitance, hence reduce the device bandwidth. By statically doping these ungated regions, analogous to p or n regions in silicon modulators, we expect to further improve the contact resistance [26, 27] and increase our extrinsic bandwidth. For example, with state-of-the-art graphene contact resistance measured as low as 100 Ω μm [28], we expect to achieve a total bandwidth of >130 GHz at cryogenic temperature with optimized graphene contacts without changing the device's cross section. Note that this high bandwidth requires ensuring that the cavity photon lifetime is not a limiting factor, which can be done by, for example, increasing the graphene capacitor length around the circumference of the ring resonator from 5 to 33 μm (see *Supplementary material*).

5 Conclusion

We have demonstrated high-speed integrated graphene modulator with measured bandwidth of 14.7 GHz with intrinsic bandwidth of 200 GHz at 4.9 K by leveraging graphene carrier mobility improvement at low temperature. In contrast to traditional electro-optic tuning mechanisms that decrease in bandwidth or modulation efficiency at low temperature, the graphene modulator exhibits an increase in electro-optic response from 293 to 4.9 K without trading off voltage or footprint. By optimizing graphene contact resistance and device footprint, we expect the graphene modulator to support bandwidths >130 GHz at cryogenic temperature. In addition, with optimized quality of gate dielectric, the modulation extinction ratio, currently limited by weaker dielectric constant and breakdown field of the Al_2O_3 gate compared with values reported in literature [29], could be further increased (see Figure S4 in the *Supplementary material*). This natural enhancement of electro-optic response at low temperature makes graphene modulators versatile and suitable for high-speed electro-optic applications at cryogenic temperature.

Methods

Please see the *Supplementary material* for detailed description of device fabrication and experimental measurements.

Acknowledgment: The authors would like to thank Dr. Min Sup Choi, Dr. Christopher T. Phare, Dr. Andres Gil-Molina, Dr. Nathan C. Abrams, Ipshita Datta, Min Chul Shin, and Euijae Shim for the fruitful discussions and experimental support. This work was performed in part at the City University of New York Advanced Science Research Center NanoFabrication Facility and in part at the Columbia Nano Initiative (CNI) shared labs at Columbia University in the City of New York.

Author contribution: All the authors have accepted responsibility for the entire content of this submitted manuscript and approved submission.

Research funding: We also gratefully acknowledge support from the Office of Naval Research for award #N00014-16-1-2219, Defense Advanced Research Projects Agency program for award #HR001110720034, National Science Foundation for award #UTA16-000936, National Aeronautics and Space Administration for award #NNX16AD16G, Air Force Office of Scientific Research for award #FA9550-18-1-0379, Air Force Materiel Command for award #FA8650-18-1-7815, and Hypres, Inc. for award #CU15-3759.

Conflict of interest statement: The authors declare no conflicts of interest regarding this article.

References

[1] M. de Cea, E. E. Wollman, A. H. Atabaki, D. J. Gray, M. D. Shaw, and R. J. Ram, "Photonic readout of superconducting nanowire single photon counting detectors," *Sci. Rep.*, vol. 10, p. 9470, 2020.

[2] A. Youssefi, I. Shomroni, Y. J. Joshi, et al., "Cryogenic electro-optic interconnect for superconducting devices," arXiv preprint arXiv: 2004.04705, 2020.

[3] M. Veldhorst, H. G. J. Eenink, C. H. Yang, and A. S. Dzurak, "Silicon CMOS architecture for a spin-based quantum computer," *Nat. Commun.*, vol. 8, no. 1, pp. 1–8, 2017.

[4] J. W. Silverstone, J. Wang, D. Bonneau, et al., "Silicon quantum photonics," in *2016 International Conference on Optical MEMS and Nanophotonics (OMN)*, IEEE, 2016, pp. 1–2.
[5] R. Maurand, X. Jehl, D. Kotekar-Patil, et al., "A CMOS silicon spin qubit," *Nat. Commun.*, vol. 7, no. 1, pp. 1–6, 2016.
[6] D. S. Holmes, A. L. Ripple, and M. A. Manheimer, "Energy-efficient superconducting computing—power budgets and requirements," *IEEE Trans. Appl. Supercond.*, vol. 23, no. 3, pp. 1701610–1701610, 2013.
[7] R. Lange, F. Heine, H. Kämpfner, and R. Meyer, "High data rate optical inter-satellite links," in *Eur. Conf. Opt. Commun.(ECOC 2009)*, Vienna, Austria, Paper, volume 10, 2009.
[8] M. Toyoshima, Y. Takayama, T. Takahashi, et al., "Ground-to-satellite laser communication experiments," *IEEE Aero. Electron. Syst. Mag.*, vol. 23, no. 8, pp. 10–18, 2008.
[9] M. Gehl, C. Long, D. Trotter, et al., "Operation of high-speed silicon photonic micro-disk modulators at cryogenic temperatures," *Optica*, vol. 4, no. 3, pp. 374–382, 2017.
[10] B. Lengeler, "Semiconductor devices suitable for use in cryogenic environments," *Cryogenics*, vol. 14, no. 8, pp. 439–447, 1974.
[11] P. Pintus, Z. Zhang, S. Pinna, et al., "Characterization of heterogeneous InP-on-Si optical modulators operating between 77 K and room temperature," *APL Photonics*, vol. 4, no. 10, p. 100805, 2019.
[12] F. Eltes, G. E. Villarreal-Garcia, D. Caimi, et al., "An integrated optical modulator operating at cryogenic temperatures," *Nat. Mater.*, pp. 1–5, 2020, https://doi.org/10.1038/s41563-020-0725-5.
[13] F. Wang, Y. Zhang, C. Tian, et al., "Gate-variable optical transitions in graphene," *Science*, vol. 320, no. 5873, pp. 206–209, 2008.
[14] Z. Q. Li, E. A. Henriksen, Z. Jiang, et al., "Dirac charge dynamics in graphene by infrared spectroscopy," *Nat. Phys.*, vol. 4, no. 7, pp. 532–535, 2008.
[15] K. I. Bolotin, K. J. Sikes, J. Hone, H. L. Stormer, and P. Kim, "Temperature-dependent transport in suspended graphene," *Phys. Rev. Lett.*, vol. 101, no. 9, p. 096802, 2008.
[16] J. H. Chen, C. Jang, S. Xiao, M. Ishigami, and M. S. Fuhrer, "Intrinsic and extrinsic performance limits of graphene devices on SiO_2," *Nat. Nanotechnol.*, vol. 3, no. 4, p. 206, 2008.
[17] W. Zhu, V. Perebeinos, M. Freitag, and P. Avouris, "Carrier scattering, mobilities, and electrostatic potential in monolayer, bilayer, and trilayer graphene," *Phys. Rev. B*, vol. 80, no. 23, p. 235402, 2009.
[18] S. Fratini and F. Guinea, "Substrate-limited electron dynamics in graphene," *Phys. Rev. B*, vol. 77, no. 19, p. 195415, 2008.
[19] M. Liu, X. Yin, E. Ulin-Avila, et al., "A graphene-based broadband optical modulator," *Nature*, vol. 474, no. 7349, pp. 64–67, 2011.
[20] A. Yariv, "Critical coupling and its control in optical waveguide-ring resonator systems," *IEEE Photonics Technol. Lett.*, vol. 14, no. 4, pp. 483–485, 2002.
[21] C. T. Phare, Y. D. Lee, J. Cardenas, and M. Lipson, "Graphene electro-optic modulator with 30 GHz bandwidth," *Nat. Photonics*, vol. 9, no. 8, pp. 511–514, 2015.
[22] W. Bogaerts, P. De Heyn, T. Van Vaerenbergh, et al., "Silicon microring resonators," *Laser Photonics Rev.*, vol. 6, no. 1, pp. 47–73, 2012.
[23] I. Gierz, J. C. Petersen, M. Mitrano, et al., "Snapshots of non-equilibrium Dirac carrier distributions in graphene," *Nat. Mater.*, vol. 12, no. 12, pp. 1119–1124, 2013.
[24] N. M. R. Peres, T. Stauber, and A. H. C. Neto, "The infrared conductivity of graphene on top of silicon oxide," *EPL (Europhysics Letters)*, vol. 84, no. 3, p. 38002, 2008.
[25] M. V. Fischetti, D. A. Neumayer, and E. A. Cartier, "Effective electron mobility in Si inversion layers in metal–oxide–semiconductor systems with a high-κ insulator: the role of remote phonon scattering," *J. Appl. Phys.*, vol. 90, no. 9, pp. 4587–4608, 2001.
[26] S. Kim, S. Shin, T. Kim, et al., "A reliable and controllable graphene doping method compatible with current CMOS technology and the demonstration of its device applications," *Nanotechnology*, vol. 28, no. 17, p. 175710, 2017.
[27] S. Vaziri, V. Chen, L. Cai, et al., "Ultrahigh doping of Graphene using flame-deposited MoO_3," *IEEE Electron Device Lett*, 2020, https://doi.org/10.1109/LED.2020.3018485.
[28] W. S. Leong, H. Gong, and J. T. L. Thong, "Low-contact-resistance graphene devices with nickel-etched-graphene contacts," *ACS Nano*, vol. 8, no. 1, pp. 994–1001, 2014.
[29] J. Yota, H. Shen, and R. Ramanathan, "Characterization of atomic layer deposition HfO_2, Al_2O_3, and plasma-enhanced chemical vapor deposition Si_3N_4 as metal–insulator–metal capacitor dielectric for GaAs HBT technology," *J. Vac. Sci. Technol. A*, vol. 31, no. 1, p. 01A134, 2013.

Supplementary Material: The online version of this article offers supplementary material (https://doi.org/10.1515/nanoph-2020-0363).